doi:10.1016/j.jmb.2006.05.033 J. Mol. Biol. (2006) 360, 882–892

JMB

Available online at www.sciencedirect.com

SCIENCE DIRECT®

ELSEVIER

Interpreting the Aggregation Kinetics of Amyloid Peptides

Riccardo Pellarin and Amedeo Caflisch*

Department of Biochemistry
University of Zürich
Winterthurerstrasse 190
CH-8057 Zürich
Switzerland

Amyloid fibrils are insoluble mainly β-sheet aggregates of proteins or peptides. The multi-step process of amyloid aggregation is one of the major research topics in structural biology and biophysics because of its relevance in protein misfolding diseases like Alzheimer's, Parkinson's, Creutzfeld-Jacob's, and type II diabetes. Yet, the detailed mechanism of oligomer formation and the influence of protein stability on the aggregation kinetics are still matters of debate. Here a coarse-grained model of an amphipathic polypeptide, characterized by a free energy profile with distinct amyloid-competent (i.e. β-prone) and amyloid-protected states, is used to investigate the kinetics of aggregation and the pathways of fibril formation. The simulation results suggest that by simply increasing the relative stability of the β-prone state of the polypeptide, disordered aggregation changes into fibrillogenesis with the presence of oligomeric on-pathway intermediates, and finally without intermediates in the case of a very stable β-prone state. The minimal-size aggregate able to form a fibril is generated by collisions of oligomers or monomers for polypeptides with unstable or stable β-prone state, respectively. The simulation results provide a basis for understanding the wide range of amyloid-aggregation mechanisms observed in peptides and proteins. Moreover, they allow us to interpret at a molecular level the much faster kinetics of assembly of a recently discovered functional amyloid with respect to the very slow pathological aggregation.

Keywords: amyloid fibril; aggregation intermediate; fibril formation kinetics; multiple pathways; Alzheimer's disease

*Corresponding author

Introduction

Amyloid fibrils are polypeptide aggregates with a core structure consisting of β-sheets whose strands are perpendicular to the fibril axis, and the backbone hydrogen bonds are parallel to it.[1] Despite the medical relevance of several diseases linked to amyloidosis, important questions about the formation kinetics of the early ordered aggregates remain unanswered. The initial phase of fibril formation is of particular interest because experimental evidence has accumulated indicating that soluble oligomeric precursors, rather than the fibrils, might be the toxic species.[2–5] However, the transient nature of oligomeric precursors makes it difficult to shed light on their formation process or structure. Additional interest in a better understanding of aggregation kinetics is being spurred by the very recent discovery of functional amyloids in mammalian cells,[6] which is challenging the view that amyloid is always cytotoxic. It is likely that aggregation kinetics have to be very fast in functional amyloids in contrast to the very slow progress of pathological protein aggregation.

Theoretical models have been developed to investigate the amyloid aggregation mechanism[7–9] and predict the rates[10] but important assumptions like the irreversible association of polypeptide chains onto the fibril[7,10] are not consistent with experimental evidence.[11,12] Computer simulations using low-resolution models, which employ a simplified representation of protein geometry and energetics, have provided insights into the basics physical principles underlying protein aggregation in general[13–15] and ordered amyloid aggregation.[16–20] Yet, they do not explain the wide range of aggregation scenarios emerging from a variety of biophysical measurements.[21,22] Computer simulations at the atomic level of detail[23–29] have shed some light on

E-mail address of the corresponding author: caflisch@bioc.unizh.ch

oligomeric aggregates and the very early steps of fibril formation. However, all-atom simulations of the kinetics of fibril formation are beyond what can be done with modern computers.

To overcome such computational limitations, we approximate a polypeptide by a coarse-grained model consisting of ten beads (Figure 1) and simulate 125 monomers in a cubic box. The monomer has internal (dihedral) flexibility and a free energy profile with two minima at the amyloid-competent state β and the amyloid-protected state π (Figure 1(d)). The latter state represents the ensemble of all polypeptide conformations that are not compatible with the cross β arrangement in a fibril, e.g. α-helical or random coil structures. An important result obtained with the coarse-grained model is that the kinetic phases and fibril formation mechanism depend on the choice of a single parameter, the relative stability of π and β states ($dE = E_\pi - E_\beta$). Notably, very different aggregation scenarios are observed by varying dE from the β-unstable ($dE \leq -2$ kcal/mol) to the β-stable ($dE \geq 0$ kcal/mol) model. The simulation results are used to interpret biophysical data on several peptides and proteins.

Results

Most of the results were obtained at a temperature of 310 K and a concentration of 8.5 mM unless specified otherwise.

Multi-step process

The range of aggregation kinetics is shown in Figures 2 and 3 while two illustrative snapshots from a simulation of the β-unstable polypeptide model ($dE = -2.5$ kcal/mol) are given in Figure 4. Three different kinetic phases are evident: lag, elongation (or growth), and final monomer-fibril equilibrium. The variable length of the lag phase and the higher heterogeneity at longer lag times are indicative of a stochastic nucleation.[30] Fibril formation is much slower for the β-unstable model than the β-stable model ($dE = 0$ kcal/mol). The model parameter dE also affects the elongation kinetics; β-unstable models display a slower elongation rate (Figure 2(b)). Interestingly, the significant anti-correlation between the length of the lag phase and the elongation rate for different values of dE is consistent with the kinetic analysis of single-point mutants of Aβ40 (compare Figure 2(a) and (b) with Figures 1 and 2 of Christopeit *et al.*,[31] respectively). The distribution function $p(N)$ of the oligomer size N evaluated at the lag phase or the final equilibrium is depicted in Figure 3. Within a given phase the peaks of the $p(N)$ distribution can be interpreted as stable oligomeric species. The monomer peak ranges from $N = 1$ to 7, the micellar peak from $N = 8$ to 60, and the fibril peak from $N = 61$ to 125. The micellar peak is present for the $dE = -2.5$ kcal/mol model at the lag phase, but disappears at the final equilibrium, where the fibril and the monomers are the only co-existing species. The height of the peaks depends on the relative stability of the β-competent state as well as the total monomer

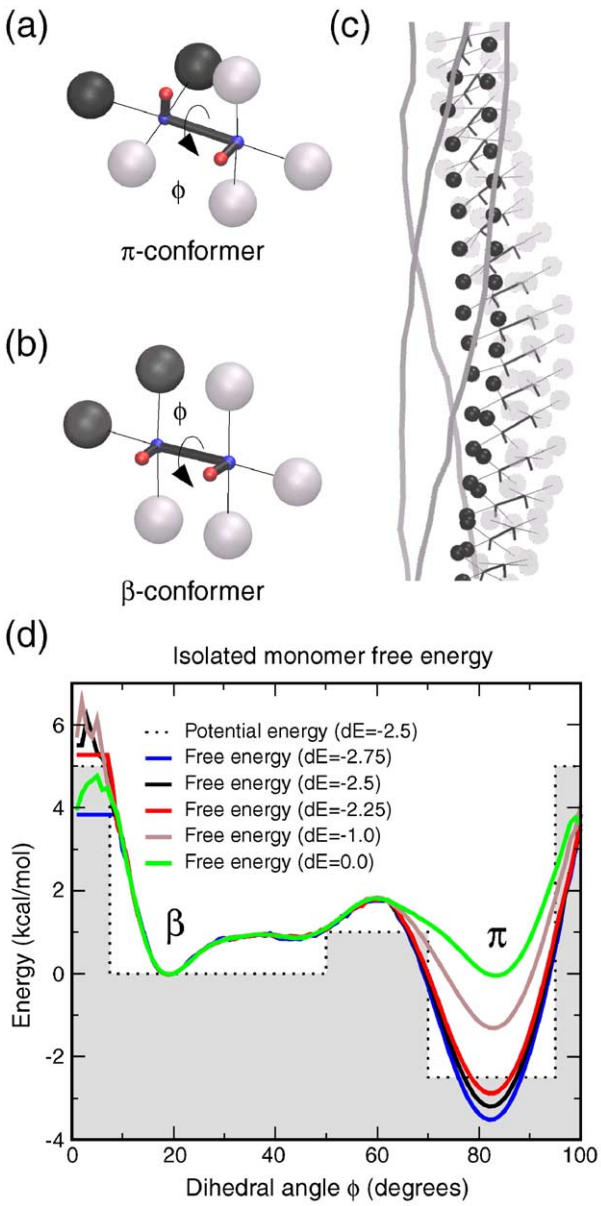

Figure 1. The model. Sticks and beads representation of the monomer in the amyloid-protected state π (a) and the amyloid-competent state β (b). The large spheres are hydrophobic (black) and hydrophilic (gray). The small red and blue spheres indicate the negative and positive partial charges that make up the "backbone" dipoles. The circular arrow indicates the rotatable bond ϕ. (c) Structure of a filament embedded in a four-filament fibril. Hydrophobic spheres are in the core of the fibril, while hydrophilic spheres are on the outside. All monomers are in the β state. The three other filaments are shown by gray ribbons. Each filament is twisted and the four filaments are intertwined. (d) The dotted line is the dihedral potential with a $dE = -2.5$ kcal/mol energy difference between amyloid-protected and amyloid-competent state. The five continuous lines represent the free energy profile of the isolated monomer for five different dihedral potentials.

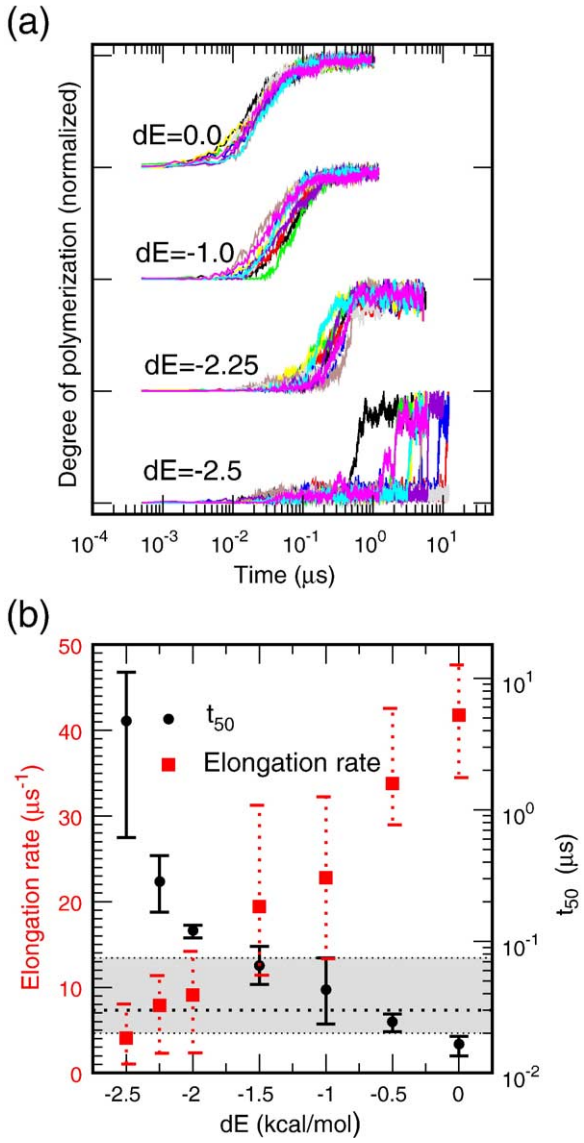

Figure 2. Effect of relative stability of the amyloid-competent state on nucleation and elongation kinetics. (a) Time series of the fraction of ordered aggregation evaluated at four values of the protected state stability dE. Ten independent simulations are shown for each dE value. The degree of polymerization is normalized to the maximum for each curve. Note that the average value at the plateau is about 10% smaller for the $dE = -2.5$ kcal/mol than the $dE = 0.0$ kcal/mol model. It is not possible to directly compare the slopes of the curves (i.e. elongation rates) at different values of dE because of the logarithmic scale of the x-axis. (b) Influence of dE on the kinetics of the system. The time needed to reach 50% of the maximal amplitude t_{50} (black circles and y-axis legend on the right) and the elongation rate (red squares and y-axis legend on the left) are displayed for seven dE values. Symbols represent the average value of ten independent runs and the error bars are the maximum and minimum values. The broken line and the gray band indicate the average and the max–min values for the time of micelle formation, respectively. All simulations were performed at a temperature of 310 K and a concentration of 8.5 mM.

concentration. For the β-stable potential $dE = 0.0$ kcal/mol the micelle peak is not observed at any concentration value. With increasing concentration the monomer and micelle peak distributions are skewed towards high N values because multi-monomer collisions and multi-micellar collisions, respectively, transiently generate oligomers of a larger size.

Micellar aggregates

Micelle-like non-fibrillar aggregates are observed only for the models with an unstable amyloid-competent state ($dE \leq -2$ kcal/mol). Furthermore, the comparison between the lag times with the time of micelle formation (gray area in Figure 2(b)) shows that the fibril formation kinetics of the β-unstable and β-stable models are slower and faster than micelle formation, respectively. In fact, micelles are intermediates consisting mainly of monomers in the π state (Figure 4(a)) whereas the polymerization of β-stable monomers directly yields fibrils. The number of monomers in the micelle is 18±5 at the concentration value of 8.5 mM and 22±8 at 62 mM, and the critical concentration of micelle formation is 4.36 mM (see Figure 5). The micellar size, its weak dependence on the concentration (see Figure 5), and the on-pathway location are in good agreement with recent fluorescence quenching data obtained for the Alzheimer's Aβ40 peptide.[32]

Mechanism of nucleation

The nucleation properties of the system are investigated by evaluating the probability of fibril formation for β-subdomains, i.e. the clusters of interacting β-monomers. The nucleus, defined as the oligomer containing a β-subdomain with a 50% probability to form a fibril, shows an increasing size upon destabilization of the β-state. The number of monomers in the nucleus is about four for the $dE = 0.0$ kcal/mol model, while it is 27 and 40 for the β-unstable models $dE = -2.25$ kcal/mol and $dE = -2.5$ kcal/mol, respectively (Figure 6(a) and (b)). Significantly different nucleation mechanisms are observed upon reduction of the relative stability of the amyloid-competent state (Figure 6(c)). In the β-stable model ($dE = 0$ kcal/mol), the nucleus size is sub-micellar and nucleation is simply the aggregation of monomers in the β-state. For the β-unstable models, nucleus formation requires either spatial proximity within a micelle of several monomers in the β-state ($dE = -2.25$ kcal/mol) or collision of two micelles with merging of their β-subdomains ($dE = -2.5$ kcal/mol). The lack of lag phase in the simulation of a "seeding experiment" (with the $dE = -2.5$ kcal/mol model, see Supplementary Data) is consistent with the nucleation dependence of the aggregation process. For the highly β-unstable model ($dE = -2.75$ kcal/mol) amyloid fibril formation is inhibited by formation of non-fibrillar aggregates having a very low density of monomers in the amyloid-competent state (Figure 6(b) and (c)).

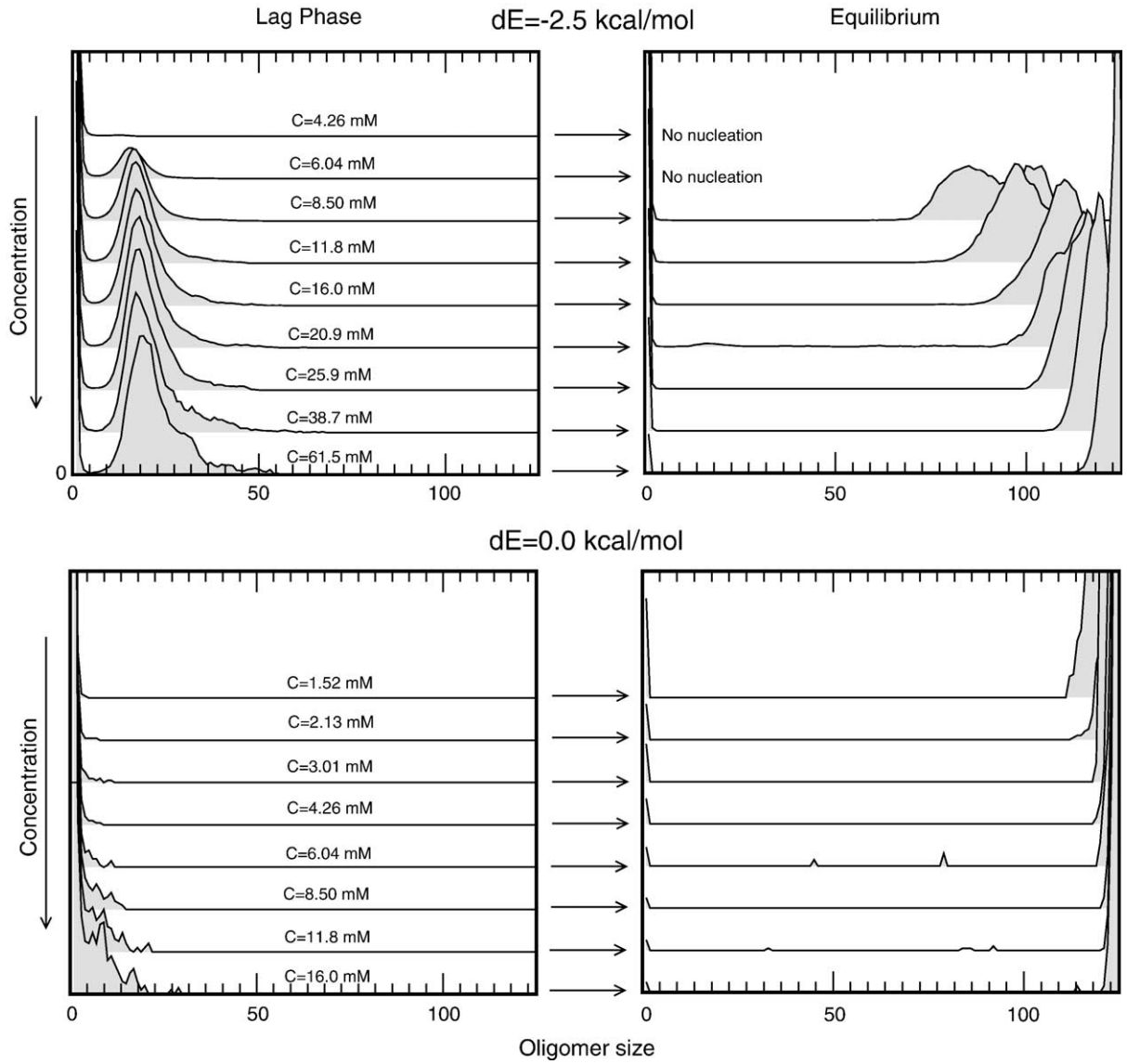

Figure 3. Oligomer size histograms of the $dE = -2.5$ kcal/mol potential (top) and $dE = 0.0$ kcal/mol potential (bottom) calculated in the lag phase (left) and the final equilibrium (right). Lag phase and equilibrium histograms evaluated at the same value of the concentration are reported in the same row. The z-dimension represents the relative probability.

Concentration effects

Another major difference between the models with unstable and stable amyloid-competent state is the dependence on the total monomer concentration of the nucleation and elongation kinetics. In agreement with the above-mentioned mechanism of nucleation, the β-unstable model nucleates only at concentration values larger than the critical concentration of micelle formation, whereas the β-stable model nucleates even at lower concentrations (Figure 7(a)). Furthermore, during the lag phase the micelle concentration increases linearly with the total monomer concentration for the β-unstable potential (see Figure 5) in agreement with neutron and light scattering data of Aβ40 during the lag phase,[33] while the concentration of dispersed monomers remains constant and equal to the critical concentration of micelle formation. Hence, the concentration dependence of the lag phase time for the β-unstable potential indicates that micelles promote the nucleation. Interestingly, the dependence of the rate of elongation on the concentration decreases significantly by increasing the stability of the protected state π (Figure 7(b)). The reduced concentration dependence originates from competitive polymerizations, i.e. the elongation of the fibril and the presence of micelles. This observation for the β-unstable model is a consequence of the monomer–micelle equilibrium, which maintains a nearly constant concentration of isolated monomers.[7]

Final monomer–fibril equilibrium

The final part of the simulations with $dE = -2.25$ or -2.5 kcal/mol is characterized by a dynamic equilibrium between monomers and fibril[11] because the micellar aggregates disappear after the elongation

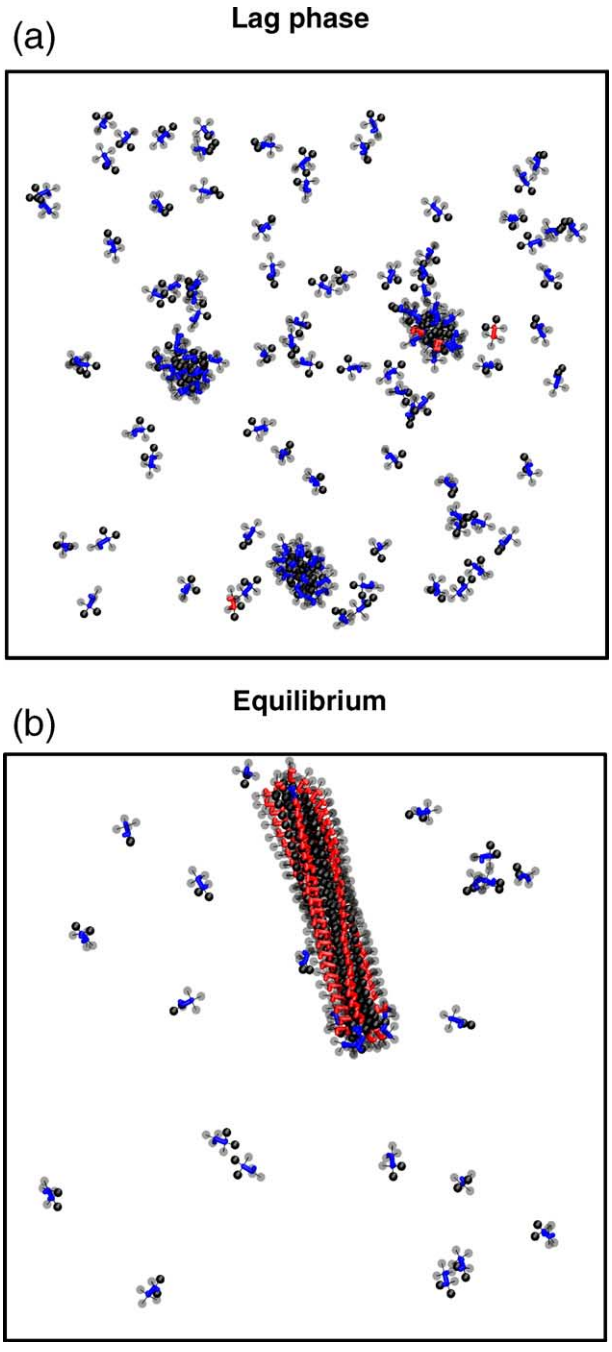

Figure 4. Kinetic phases for the β-unstable model. Snapshots from the lag phase (a) and the final monomer–fibril equilibrium (b) for a simulation with $dE = -2.5$ kcal/mol and 8.5 mM concentration. Hydrophobic and hydrophilic spheres are black and gray, respectively. The backbone is blue for π-state monomers and red for β-state monomers to emphasize that micelles consist mainly of the former (a) whereas the fibril is made up of the latter (b).

phase (Figures 3 and 4). Fibrils consist of bundles of four intertwined filaments (Figures 1(c) and 4(b)). Their caps are disordered and host monomers in the π state whose population correlates with the relative stability of the π *versus* β state. The final equilibrium observed in the coarse-grained model simulations indicates that the assumption of irreversible association of polypeptide chains onto the fibril[10] is not justified. Recently, a molecular recycling mechanism has been observed by a combination of NMR spectroscopy and mass spectroscopy for an amyloid fibril formed from an SH3 domain.[12] To evaluate the recycling time of the coarse-grained model, simulations of mature fibrils in equilibrium with dispersed monomers are analyzed for the β-unstable potential ($dE = -2.5$ kcal/mol) at different concentration values by monitoring the number of the unrecycled monomers $N_u(t)$ (Figure 8). In two of nine simulations, $N_u(t)$ goes to zero within 4 μs showing that all monomers initially belonging to the fibril have been recycled. The time for recycling half of the monomers incorporated into a fibril is of the order of 2–20 μs and is independent of the total monomer concentration (see inset of Figure 8). Such "molecular recycling" indicates that, despite their ordered arrangement, fibrils are dynamic assemblies.

Discussion

The detailed description of the kinetics and thermodynamics of the coarse-grained model suggests some general conclusions concerning the aggregation mechanism of amyloidogenic peptides and proteins. The striking variety of fibril formation mechanisms mainly depends on the relative stability of the amyloid-competent state of the monomer. Despite the essentially identical structure of the final fibril, ordered aggregation of the β-stable model follows a downhill pathway[34,35] without intermediates,

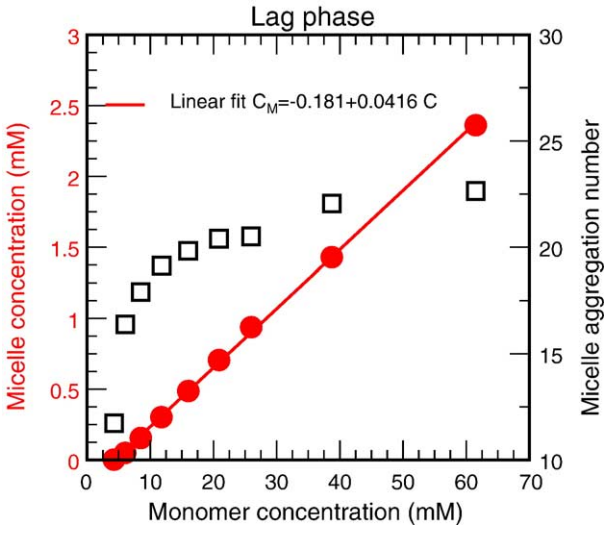

Figure 5. Lag phase of the $dE = -2.5$ kcal/mol potential. The micelle concentration C_M (red circles, *y*-axis, legend on the left) shows a linear increase when plotted as a function of the total concentration of monomers, *C*. The red continuous line is a linear fit whose parameters are reported in the graph. The *x*-axis intercept of the red continuous line is the critical concentration of micelle formation (4.36 mM). The micelle aggregation number (squares, *y*-axis, legend on the right) reaches a plateau at monomer concentration larger than 20 mM.

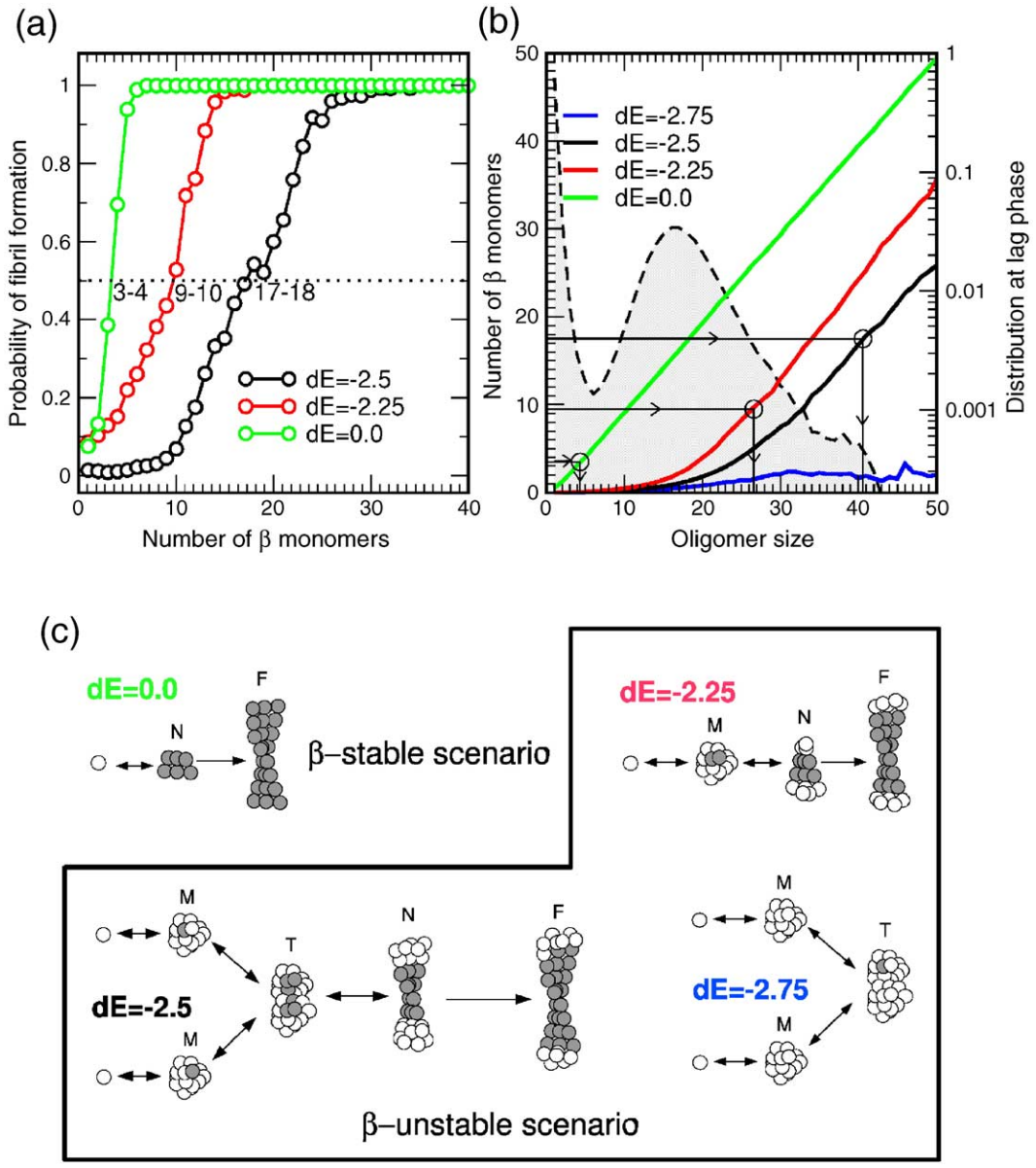

Figure 6. (a) Probability of fibril formation as a function of the size of the β-subdomain evaluated for three different dE values at a concentration of 8.5 mM. The integer ranges close to the dotted line are the β-subdomain sizes at probability equal to 0.5 (see the text for nucleus definition). (b) Average number of β-state monomers as a function of the oligomer size. The β-subdomain sizes of the left plot are reported in ordinate and the corresponding oligomer sizes are indicated by arrows. As an example, for $dE = -2.25$ kcal/mol, the nucleus consists of a β-subdomain of size 9–10 incorporated in a micelle of about 27 monomers. The broken line is the oligomer size distribution calculated at the lag phase for $dE = -2.5$ kcal/mol and concentration of 8.5 mM (see Figure 3). (c) Observed nucleation scenarios. Black and white circles represent the amyloid-competent conformer β and amyloid-protected conformer π, respectively. β-Stable monomers nucleate without intermediates, while β-unstable monomers can nucleate either through micelle-sized oligomers ($dE = -2.25$) or transient oligomers larger than micelle ($dE = -2.5$). A further stabilization of the protected state prevents fibril formation ($dE = -2.75$). M, micelle; N, nucleus; T, transient oligomer; F, fibril.

while fibrillization of the β-unstable model occurs with the presence of on-pathway oligomers. In other words, high and low β-prone sequences show completely different kinetic behaviors. This simulation result provides a basis to understand the more than four orders of magnitude faster kinetic assembly of a functional amyloid with respect to Aβ under identical experimental conditions.[6]

An unstructured peptide with a marginally stable β-prone state (e.g. Aβ40[32,36] or the islet amyloid polypeptide[37]) as well as the α/β protein acylphosphatase[22] visit oligomeric systems in the lag phase, and have a very weak dependence of the elongation rate on concentration due to the monomer–micelle equilibrium. This mechanism corresponds to the nucleated conformational conversion proposed by Serio *et al.*[38] Other examples of the β-unstable model include phosphoglycerate kinase (PGK), an α/β protein, which was investigated by light scattering, circular dichroism and electron

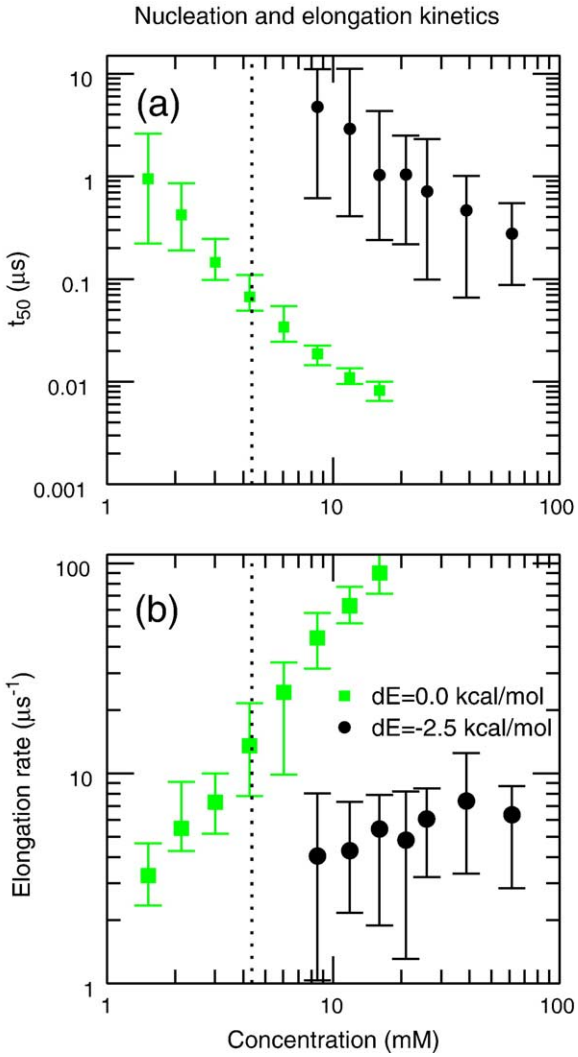

Figure 7. (a) Effect of concentration on the lag phase time t_{50} for β-unstable $dE = -2.5$ kcal/mol (black circles) and β-stable $dE = 0.0$ kcal/mol (green squares) models. The symbols represent the average value calculated on 15 simulations for $dE = -2.5$ and ten simulations for $dE = 0.0$. The error bars represent the minimum and the maximum value. (b) Effect of concentration on the elongation rate of the fibril. Symbols and error bars are as for (a). The vertical dotted line indicates the critical concentration of micelle formation.

microscopy. The amyloid formation of PGK was shown to be a two-stage process where critical oligomers with low β content assembly to form protofibril and fibrils of increasing cross-β structure.[9] A similar mechanism was proposed by Xu *et al.* for the full length yeast prion-like protein Sup35 using atomic force microscopy.[39] Both aforementioned mechanisms are described by the β-unstable model, which is observed to nucleate through an isolated micelle or transiently associated micelles (Figure 4(c)). On the other hand, a functional and non-pathological amyloid in mammalians[6] as well as oligopeptides with amyloid-prone sequence (e.g. the heptapeptide GNNQQNY from the N-terminal domain of the Sup35,[40,41] or the blocked diphenylalanine[42]) lack on-pathway intermediates and correspond to the β-stable model. Most importantly, it is not necessarily the stability of the folded structure, as suggested recently,[35,43] to determine the aggregation mechanism but rather the relative stability of the β-prone state.[44] In fact, the simulation results can be used to interpret the different kinetic behaviors even within proteins with stable native fold. Transthyretin[35] and β_2-microglobulin[21] have a β-sheet-rich folded state and show downhill polymerization (depending on the solution conditions) because of the intrinsic β-propensity of their sequences, as observed for the β-stable model. On the contrary, mainly α-helical structures like myoglobin and the prion protein require extreme environmental conditions (high temperature for apomyoglobin)[45] and show a significant lag phase as observed for the β-unstable models. Furthermore, the importance of the relative stability of the β-prone state is consistent with the experimental observation that the changes in nucleation and elongation kinetics upon single point mutations correlate more with the β-propensity and the hydrophobicity[46,47] than the α-helical stability as recently reported for Aβ40.[31] However, the possibility to change solely the intrinsic conformational landscape of a monomer without affecting the inter-monomer non-covalent interactions represent an advantage of the coarse-grained model and simulation approach with respect to experimental methods such as mutagenesis and solvent-induced conformational changes, by which it is not possible to separate the two effects. For instance, mutation of the Aβ40 peptide, even a single point substitution, can have an influence on both the energy landscape

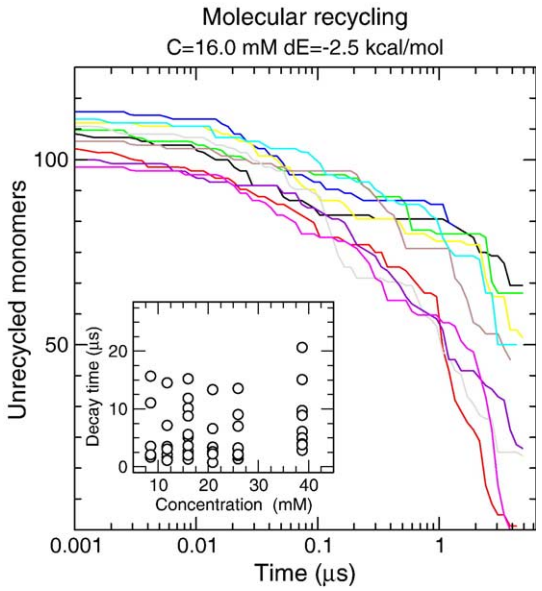

Figure 8. Number of unrecycled monomers N_u as a function of time for nine simulations started from a preformed equilibrated fibril. Simulations were performed at total concentration $C = 16.0$ mM and for the $dE = -2.5$ kcal/mol model. The values of the decay time τ (i.e. the time to reach $e^{-1}N_u(0)$) at different concentrations are reported in the inset.

of the monomer and the intermolecular forces. In conclusion, a slight modification of the free energy profile is sufficient to observe a wide range of different fibril formation mechanisms providing a unifying description of the available experimental results. This finding has significant implications for the design of drugs against amyloid diseases as well as for the production of nanofibrillar materials.[48]

Materials and Methods

Model

A monomer consists of ten spherical beads arranged to have an overall amphipathic character. The relative stability of the amyloid-competent (β) and amyloid-protected (π) state is modulated by varying the dihedral energy difference of the single rotatable bond of the monomer. Interactions between monomers depend on van der Waals and electrostatic forces (Figure 1). The former approximate both steric and hydrophobic effects while the latter are dipole–dipole interactions responsible for the ordered stacking of monomers incorporated in the fibril. Details of the model are given in the Supplementary Data.

Simulation protocol

Disordered aggregation and/or fibril formation is simulated at physiological temperature (310 K) by following the time evolution (Langevin dynamics) of 125 monomers enclosed in a cubic box, at constant volume conditions, and starting from a monodisperse solution. Periodic boundary conditions are applied to avoid finite size effects. The total monomer concentration of 8.5 mM is about two orders of magnitude higher than the reported experimental concentrations of 30 μM −300 μM. The very high peptide concentration is used to increase the probability of intermolecular interactions, making the oligomerization process fast enough to be observed in a simulation time scale of about 10 μs, which requires about 25 days of CPU time. All simulations were performed with CHARMM.[49]

Dihedral free energy profile

The dihedral free energy profile reported in Figure 1(d) is evaluated for an isolated monomer as follows:

$$\Delta G(\phi) = -kT \log\left(\frac{n(\phi)}{n(\phi = 20^\circ)}\right)$$

where $n(\phi)$ is the probability to assume a dihedral angle equal to ϕ. The β-state minimum at $\phi = 20^\circ$ is taken as reference.

Oligomer size distribution

A clustering algorithm is used to calculate the size of the oligomeric species along the simulations. It is based on the matrix of contacts D_{ij} between labeled monomers. Given a single frame of the simulation, D_{ij} is equal to one if any sphere of monomer i is closer than 6.0 Å to any sphere of monomer j, otherwise it is zero. D_{ij} is equivalent to the first neighbor matrix, $d_{ij}^{(1)}$. The second neighbor matrix $d^{(2)}$ is constructed from $d^{(1)}$ including the neighbors of the first neighbors. The converged contact matrix $d_{ij}^{(\infty)}$ is defined by the following recursive sequence:

$$d_{ij}^{(1)} = D_{ij}$$

$$d_{ij}^{(n)} = \begin{cases} 1 & \text{if} \quad d_{ij}^{(n-1)} = 1 \\ 1 & \text{if} \quad d_{ik}^{(n-1)} = 1 \text{ and } d_{kj}^{(n-1)} = 1 \\ 0 & \text{otherwise} \end{cases}$$

$$d_{ij}^{(\infty)} = \lim_{n \to \infty} d_{ij}^{(n)}$$

which yields a block matrix of ones and zeroes. Each block represents a cluster of monomers and contains first neighbors, second neighbors, third and so on. This procedure is equivalent to a hierarchical clustering performed with a spanning tree technique.[50] With the converged contact matrix one can identify clusters (i.e. tagging each oligomer with an identification number), list monomers belonging to a specific oligomer and make statistics on the size of oligomers. The above definition of oligomeric species allows the statistical analysis of cluster size. The probability that a monomer is aggregated in a cluster of size N is:

$$p(N) = \left\langle \frac{1}{N_T} \sum_{i=1,N_T} \delta_{i,t}(N) \right\rangle_t$$

where N_T is the total number of simulated monomers, $\delta_{i,t}(N)$ is equal to 1 if the monomer i at time t is embedded in a cluster of size N, and the angular brackets are the time average. This function (termed oligomer size distribution) can be evaluated for the lag phase or the final monomer–fibril equilibrium. The elongation phase cannot be analyzed by $p(N)$ being an out of equilibrium dynamic process.

Critical concentration of micelle formation

The probability distribution $p(N)$ can be used to evaluate the critical concentration of micelle formation C^r_M. The micelle aggregation number in the lag phase is defined as:

$$N_M = \sum_{N=8}^{60} N p^{lp}(N)$$

where p^{lp} is the function $p(N)$ evaluated only in the lag phase (where there is co-existence of micelles and monomers without fibrils). The number of micelles per simulation box is $N_T p_M N_M^{-1}$, where the total number of simulated monomers N_T is 125 and p_M is the probability of a monomer being in a micelle. The micelle concentration C_M is derived from the number of micelles in the simulation volume. The micelle aggregation number N_M and concentration are plotted in Figure 5 as a function of the total monomer concentration C for the potential $dE = -2.5$ kcal/mol in the lag phase. By extrapolating a linear fit of the concentration of micelles the critical concentration of micelle formation C^r_M can be evaluated. The value is $C^r_M = 4.36$ mM.

Kinetics

The time series displayed in Figure 2(a) are evaluated by counting the number of parallel polar contacts n_p, i.e. the number of inter-monomer dipole–dipole interactions normalized to the maximum value. This observable is

approximately zero at the lag phase and increases with the degree of fibril polymerization after the nucleation. The elongation rate (Figures 2(b) and 7(b)) is evaluated by fitting the n_p time series with an exponential function, whereas t_{50} (Figures 2(b) and 7(a)) is the time needed to reach 50% of the maximum n_p amplitude. Time series of the number of inter-monomer hydrophobic contacts n_h are used to calculate the time of micelle formation (gray band in Figure 2(b)), which is the time needed to reach 50% of the amplitude at the lag phase starting from initially dissolved monomers ($n_h = 0$). See Supplementary Data for additional information.

Probability of fibril formation

β-Subdomains, defined as clusters of interacting β-monomers, are used to evaluate the probability of fibril formation shown in Figure 6(a). Given a β-subdomain A_{N_β} of size N_β, the set of pathways P_i is defined as the set of β-subdomain trajectories produced starting from A_{N_β}. The probability of fibril formation for a β-subdomain of size N_β is defined as:

$$p_{Ff}(N_\beta) = \frac{1}{M}\sum_{P_i} F(P_i)$$

where M is a normalization term that accounts for the occurrence of oligomer A_{N_β} in the simulations, and $F(P_i)$ is equal to 1 if the pathway produces a fiber, and otherwise it is 0. The number of β-monomers in an oligomer of size N, reported in Figure 6(b), is calculated from the free energy difference between the β and π states in an oligomer of size N, $\Delta G_{\beta\pi}(N)$:

$$N_\beta(N) = \frac{N e^{\frac{\Delta G_{\beta\pi}(N)}{kT}}}{1 + e^{\frac{\Delta G_{\beta\pi}(N)}{kT}}}$$

See Supplementary Data for additional information.

Number of unrecycled monomers

The number of unrecycled monomers $N_u(t)$ is defined as follows. First, all monomers belonging to the fibril at time $t = 0$ are labeled and counted. Then, at all times $t > 0$ the monomers that never detached from the fibril are counted and the resulting number is $N_u(t)$. The number of unrecycled monomers $N_u(t)$ can be fitted with an exponential function:

$$N_u(t) = N_u(0)e^{-t/\tau}$$

where $N_u(0)$. is the initial value of monomers belonging to the fibril and τ is the decay time.

Acknowledgements

We thank Dr A. Cavalli, Dr M. Cecchini, Dr E. Guarnera and Dr G. Tartaglia for interesting discussions, and Dr S. Bernèche, Professor R. Melki and Professor B. Schuler for useful comments on the manuscript. The calculations were performed on Matterhorn, a Beowulf Linux cluster at the Informatikdienste of the University of Zurich, and we thank C. Bolliger, Dr T. Steenbock, and Dr A. Godknecht for installing and maintaining the Linux cluster. This work was supported by the Swiss National Competence Center in Research (NCCR) on Neural Plasticity and Repair.

Supplementary Data

Supplementary data associated with this article can be found, in the online version, at doi:10.1016/j.jmb.2006.05.033

References

1. Sunde, M. & Blake, C. (1997). The structure of amyloid fibrils by electron microscopy and X-ray diffraction. *Adv. Protein Chem.* **50**, 123–159.
2. Conway, K. A., Lee, S. J., Rochet, J. C., Ding, T. T., Williamson, R. E. & Lansbury, P. T. J. (2000). Acceleration of oligomerization, not fibrillization, is a shared property of both alpha-synuclein mutations linked to early-onset Parkinson's disease: implications for pathogenesis and therapy. *Proc. Natl Acad. Sci. USA*, **97**, 571–576.
3. Bucciantini, M., Giannoni, E., Chiti, F., Baroni, F., Formigli, L., Zurdo, J. *et al.* (2002). Inherent toxicity of aggregates implies a common mechanism for protein misfolding diseases. *Nature*, **416**, 507–511.
4. Kayed, R., Head, E., Thompson, J. L., McIntire, T. M., Milton, S. C., Cotman, C. W. & Glabe, C. G. (2003). Common structure of soluble amyloid oligomers implies common mechanism of pathogenesis. *Science*, **300**, 486–489.
5. Cleary, J. P., Walsh, D. M., Hofmeister, J. J., Shankar, G. M., Kuskowski, M. A., Selkoe, D. J. & Ashe, K. H. (2005). Natural oligomers of the amyloid-beta protein specifically disrupt cognitive function. *Nature Neurosci.* **8**, 79–84.
6. Fowler, D. M., Koulov, A. V., Alory-Jost, C., Marks, M. S., Balch, W. E. & Kelly, J. W. (2006). Functional amyloid formation within mammalian tissue. *PLoS Biol.* **4**, e6.
7. Lomakin, A., Teplow, D. B., Kirschner, D. A. & Benedek, G. (1997). Kinetic theory of fibrillogenesis of amyloid β-protein. *Proc. Natl Acad. Sci. USA*, **94**, 7942–7947.
8. Massi, F. & Straub, J. E. (2001). Energy landscape theory for Alzheimer's amyloid β-peptide fibril elongation. *Proteins: Struct. Funct. Bioinformat.* **42**, 217–229.
9. Modler, A. J., Gast, K., Lutsch, G. & Damaschun, G. (2003). Assembly of amyloid protofibrils *via* critical oligomers–a novel pathway of amyloid formation. *J. Mol. Biol.* **325**, 135–148.
10. Hall, D., Hirota, N. & Dobson, C. M. (2005). A toy model for predicting the rate of amyloid formation from unfolded protein. *J. Mol. Biol.* **351**, 195–205.
11. O'Nuallain, B., Shivaprasad, S., Kheterpal, I. & Wetzel, R. (2005). Thermodynamics of Aβ(1–40) amyloid fibril elongation. *Biochemistry*, **44**, 12709–12718.
12. Carulla, N., Caddy, G. L., Hall, D. R., Zurdo, J., Gairi, M., Feliz, M. *et al.* (2005). Molecular recycling within amyloid fibrils. *Nature*, **436**, 554–558.
13. Broglia, R. A., Tiana, G., Pasquali, S., Roman, H. E. & Vigezzi, E. (1998). Folding and aggregation of

designed proteins. *Proc. Natl Acad. Sci. USA*, **95**, 12930–12933.
14. Gupta, P., Hall, C. K. & Voegler, A. C. (1998). Effect of denaturant and protein concentrations upon protein refolding and aggregation: a simple lattice model. *Protein Sci.* **7**, 2642–2652.
15. Harrison, P. M., Chan, H. S., Prusiner, S. B. & Cohen, F. E. (1999). Thermodynamics of model prions and its implications for the problem of prion protein folding. *J. Mol. Biol.* **286**, 593–606.
16. Urbanc, B., Cruz, L., Yun, S., Buldyrev, S. V., Bitan, G., Teplow, D. B. & Stanley, H. E. (2004). *In silico* study of amyloid beta-protein folding and oligomerization. *Proc. Natl Acad. Sci. USA*, **101**, 17345–17350.
17. Nguyen, H. D. & Hall, C. K. (2004). Molecular dynamics simulations of spontaneous fibril formation by random-coil peptides. *Proc. Natl Acad. Sci. USA*, **101**, 16180–16185.
18. Jang, H., Hall, C. K. & Zhou, Y. (2004). Assembly and kinetic folding pathways of a tetrameric beta-sheet complex: molecular dynamics simulations on simplified off-lattice protein models. *Biophys. J.* **86** (1 Pt 1), 31–49.
19. Dima, R. I. & Thirumalai, D. (2002). Exploring protein aggregation and self-propagation using lattice models: phase diagram and kinetics. *Protein Sci.* **11** (5), 1036–1049.
20. Malolepsza, E., Boniecki, M., Kolinski, A. & Piela, L. (2005). Theoretical model of prion propagation: a misfolded protein induces misfolding. *Proc. Natl Acad. Sci. USA*, **102**, 7835–7840.
21. Gosal, W. S., Morten, I. J., W., H. E., Smith, D. A., Thomson, N. H. & Radford, S. E. (2005). Competing pathways determine fibril morphology in the self-assembly of β_2-microglobulin into amyloid. *J. Mol. Biol.* **351**, 850–864.
22. Plakoutsi, G., Bemporad, F., Calamai, M., Taddei, N., Dobson, C. M. & Chiti, F. (2005). Evidence for a mechanism of amyloid formation involving molecular reorganisation within native-like precursor aggregates. *J. Mol. Biol.* **351**, 910–922.
23. Ma, B. & Nussinov, R. (2002). Stabilities and conformations of Alzheimer's β-amyloid peptide oligomers ($A\beta_{16-22}$, $A\beta_{16-35}$, and $A\beta_{10-35}$): sequence effects. *Proc. Natl Acad. Sci. USA*, **99**, 14126–14131.
24. Gsponer, J., Haberthür, U. & Caflisch, A. (2003). The role of side-chain interactions in the early steps of aggregation: molecular dynamics simulations of an amyloid-forming peptide from the yeast prion Sup35. *Proc. Natl Acad. Sci. USA*, **100**, 5154–5159.
25. Klimov, D. & Thirumalai, D. (2003). Dissecting the assembly of A amyloid peptides into antiparallel β sheets. *Structure*, **11**, 295–307.
26. Wei, G., Mousseau, N. & Derreumaux, P. (2004). Sampling the self-assembly pathways of KFFE hexamers. *Biophys. J.* **87**, 3648–3656.
27. Hwang, W., Zhang, S., Kamm, R. D. & Karplus, M. (2004). Kinetic control of dimer structure formation in amyloid fibrillogenesis. *Proc. Natl Acad. Sci. USA*, **101**, 12916–12921.
28. Buchete, N.-V., Tycko, R. & Hummer, G. (2005). Molecular dynamics simulations of Alzheimer's beta-amyloid protofilaments. *J. Mol. Biol.* **353**, 804–821.
29. Lopez de la Paz, M., de Mori, G. M. S., Serrano, L. & Colombo, G. (2005). Sequence dependence of amyloid fibril formation: insights from molecular dynamics simulations. *J. Mol. Biol.* **349**, 583–596.
30. Hortschansky, P., Schroeckh, V., Christopeit, T., Zandomeneghi, G. & Fändrich, M. (2005). The aggregation kinetics of Alzheimer's beta-amyloid peptide is controlled by stochastic nucleation. *Protein Sci.* **14**, 1753–1759.
31. Christopeit, T., Hortschansky, P., Schroeckh, V., Guhrs, K., Zandomeneghi, G. & Fändrich, M. (2005). Mutagenic analysis of the nucleation propensity of oxidized Alzheimer's beta-amyloid peptide. *Protein Sci.* **14**, 2125–2131.
32. Sabate, R. & Estelrich, J. (2005). Evidence of the existence of micelles in the fibrillogenesis of β-amyloid peptide. *J. Phys. Chem. ser. B*, **109**, 11027–11032.
33. Yong, W., Lomakin, A., Kirkitadze, M. D., Teplow, D. B., Chen, S.-H. & Benedek, G. B. (2002). Structure determination of micelle-like intermediates in amyloid beta -protein fibril assembly by using small angle neutron scattering. *Proc. Natl Acad. Sci. USA*, **99**, 150–154.
34. Prusiner, S. B. (1991). Molecular biology of prion diseases. *Science*, **252**, 1515–1522.
35. Hurshman, A. R., White, J. T., Powers, E. T. & Kelly, J. W. (2004). Transthyretin aggregation under partially denaturing conditions is a downhill polymerization. *Biochemistry*, **43**, 7365–7381.
36. Lomakin, A., Chung, D. S., Benedek, G. B., Kirschner, D. A. & Teplow, D. B. (1996). On the nucleation and growth of amyloid beta-protein fibrils: detection of nuclei and quantitation of rate constants. *Proc. Natl Acad. Sci. USA*, **93**, 1125–1129.
37. Rhoades, E. & Gafni, A. (2003). Micelle formation by a fragment of human islet amyloid polypeptide. *Biophys. J.* **84**, 3480–3487.
38. Serio, T. R., Cashikar, A. G., Kowal, A. S., Sawicki, G. J., Moslehi, J. J., Serpell, L. *et al.* (2000). Nucleated conformational conversion and the replication of conformational information by a prion determinant. *Science*, **289**, 1317–1321.
39. Xu, S., Bevis, B. & Arnsdorf, M. F. (2001). The assembly of amyloidogenic yeast sup35 as assessed by scanning (atomic) force microscopy: an analogy to linear colloidal aggregation? *Biophys. J.* **81**, 446–454.
40. Balbirnie, M., Grothe, R. & Eisenberg, D. (2001). An amyloid-forming peptide from the yeast prion Sup35 reveals a dehydrated β-sheet structure for amyloid. *Proc. Natl Acad. Sci. USA*, **98**, 2375–2380.
41. Nelson, R., Sawaya, M., Balbirnie, M., Grothe, R. & Eisenberg, D. (2005). Structure of the cross-β-spine of amyloid-like fibrils. *Nature*, **435**, 773–778.
42. Reches, M. & Gazit, E. (2005). Self-assembly of peptide nanotubes and amyloid-like structures by charged-termini-capped diphenylalanine peptide analogues. *Israel J. Chem.* **45**, 363–371.
43. Cohen, F. & Kelly, J. W. (2003). Therapeutic approaches to protein-misfolding diseases. *Nature*, **426**, 905–909.
44. Thirumalai, D., Klimov, D. K. & Dima, R. I. (2003). Emerging ideas on the molecular basis of protein and peptide aggregation. *Curr. Opin. Struct. Biol.* **13**, 146–159.
45. Fändrich, M., Forge, V., Buder, K., Kittler, M., Dobson, C. M. & Diekmann, S. (2003). Myoglobin forms amyloid fibrils by association of unfolded polypeptide segments. *Proc. Natl Acad. Sci. USA*, **100**, 15463–15468.
46. Chiti, F., Stefani, M., Taddei, N., Ramponi, G. & Dobson, C. M. (2003). Rationalization of the effects of mutations on peptide and protein aggregation rates. *Nature*, **424**, 805–808.
47. Tartaglia, G. G., Cavalli, A., Pellarin, R. & Caflisch, A. (2004). The role of aromaticity, exposed surface, and

dipole moment in determining protein aggregation rates. *Protein Sci.* **13**, 1939–1941.
48. Hamada, D., Yanagihara, I. & Tsumoto, K. (2004). Engineering amyloidogenicity towards the development of nanofibrillar materials. *Trends Biotechnol.* **22**, 93–97.
49. Brooks, B. R., Bruccoleri, R. E., Olafson, B. D., States, D. J., Swaminathan, S. & Karplus, M. (1983). CHARMM: a program for macromolecular energy, minimization, and dynamics calculations. *J. Comput. Chem.* **4**, 187–217.
50. Johnson, S. C. (1967). Hierarchical clustering schemes. *Psychometrika*, **32**, 241–254.

Edited by F. E. Cohen

(Received 22 February 2006; accepted 6 May 2006)
Available online 5 June 2006